Nuclear Engineering and Technology 53 (2021) 258–265

Contents lists available at ScienceDirect

Nuclear Engineering and Technology

journal homepage: www.elsevier.com/locate/net

Original Article

Application of sigmoidal optimization to reconstruct nuclear medicine image: Comparison with filtered back projection and iterative reconstruction method

Han-Back Shin [a], Moo-Sub Kim [b], Martin Law [c], Shih-Kien Djeng [c], Min-Geon Choi [b], Byung Wook Choi [d], Sungmin Kang [d], Dong-Wook Kim [a], Tae Suk Suh [b, **, 1], Do-Kun Yoon [b, *, 1]

[a] Department of Radiation Oncology, Yonsei Cancer Center, Yonsei University, College of Medicine, Seoul, 03722, South Korea
[b] Department of Biomedical Engineering and Research Institute of Biomedical, Engineering, College of Medicine, Catholic University of Korea, Seoul, 06591, South Korea
[c] Proton Therapy Pte Ltd, 1 Biopolis Drive, 138622, Singapore
[d] Department of Nuclear Medicine, Daegu Catholic University Medical Center, Catholic University of Daegu School of Medicine, Daegu, 42471, South Korea

ARTICLE INFO

Article history:
Received 18 March 2020
Received in revised form
19 June 2020
Accepted 24 June 2020
Available online 27 July 2020

Keywords:
Sigmoid function
Profile optimization
PET
SPECT
Monte Carlo simulation

ABSTRACT

High levels for noise and a loss of true signal make the quantitative interpretation of nuclear medicine (NM) images difficult. An application of profile optimization using a sigmoidal function in this study was used to acquire the NM images with high quality. And the images were acquired by using three kinds of reconstruction method using each same sinogram: a standard filtered back-projection (FBP), an iterative reconstruction (IR) technique, and the sigmoidal function profile optimization (SFPO). Comparison of image according to reconstruction method was performed to show a superiority of the SFPO for imaging. The images reconstructed by using the SFPO showed an average of 1.49 times and of 1.17 times better in contrast than the results obtained using the standard FBP and the IR technique, respectively. Higher signal to noise ratios were obtained as an average of 12.30 times and of 3.77 times than results obtained using the standard FBP and the IR technique, respectively. This study confirms that reconstruction with SFPO (*vs* FBP and *vs* IR) can lead to better lesion detectability and characterization with noise reduction. It can be developed for future reconstruction technique for the NM imaging.

1. Introduction

Nuclear medicine (NM) imaging technique is a representative molecular imaging method using of a radiopharmaceutical compound, which may be accumulated into a tumor region after patient injection. The NM images can be then acquired with the use of a single photon emission computed tomography (SPECT) or of a positron emission tomography (PET) [1]. This detected gamma ray events are used to generate a sinogram representing the raw data for the NM images [2], the image reconstructions of which are commonly performed with the use of standard filtered back projection (FBP) or of the iterative type ordered subset expectation maximization (OSEM) algorithm in the commercialized product [2]. The type of the image reconstruction algorithms can affect the quality and quantification of the reconstructed NM images. Moreover, the acquisition time of the images can be dependent upon these type of the algorithm [3]. For this reason, there has been continuous development of the reconstruction algorithm in patient imaging [4,5]. The representative conventional reconstruction algorithm for the NM imaging is the standard FBP algorithm [6], in which the blurring effect at the image edge can be removed by using a specific filter. Nevertheless, the overall noise level embedded within the image still remains. The high noise level and the reduced signal level lead the difficulty for the image interpretation. On the other hand, an iterative reconstruction method based on the probability model such as the Poisson distribution has been proposed for the innovative noise reduction [7–12]. When the

* Corresponding author.
** Corresponding author.
E-mail addresses: suhsanta@catholic.ac.kr (T.S. Suh), dbsehrns@naver.com (D.-K. Yoon).
[1] These authors have contributed equally to this work.

https://doi.org/10.1016/j.net.2020.06.029

OSEM method is used to reconstruct the NM images, the signal level is increased and noise level is decreased according to the probability with the iterative works [13–18]. Because the OSEM algorithm allows the distribution of the calculation for acquiring the image by the assignment of the subset, the image acquisition time can be reduced [3]. However, the problem regarding the signal loss resulted from increasing number of iterations is still unsolved even with the use of the graphic processing unit (GPU) to acquire the NM images [19,20]. In order to solve the problem for the signal loss, there have been a lot of trials in the field of medical imaging [21–30]. Nevertheless, we propose to use a model of 'loss function' to acquire the NM image. Although the loss function is originally a criterion of an evaluation to show an accuracy of a hypothesis for a regression, these characteristics can be applied to change the specific arrangement to the ideal pattern [31]. The sigmoidal function, being a curve with letter 'S' in shape, is a representative model of the loss function. This sigmoidal function has been applied to several research areas such as curve fitting and electronic signal analysis [31,32]. The ideal pattern of the profile for the NM image looks like a sharp sigmoidal function. If the rough profile from the image can be changed as the ideal pattern such as the sharp sigmoidal function with the 'clear criteria', the quality of the image will be accordingly increased. However, in order to establish the clear criteria, the information of a tendency should be required. This tendency can be defined with the weighting parameter. The specific weighting parameters to optimize the original values should be extracted from large dataset [33–36]. Values of the curve gradient along the sigmoidal function are used as reference values for the weighting parameters and the NM image profiles will be optimized accordingly. The re-arrangement of these optimized profiles can reconstruct the NM images close to their true patterns. The purpose of this study is to propose an image reconstruction method using sigmoidal function and to compare the image quality with that of the standard FBP as well as the iterative reconstruction technique using the quantitative analysis.

2. Materials and methods

2.1. System description and data acquisition

To acquire a relation between the quality of NM images and image acquisition technique, imaging machines of SPECT and PET were simulated using the Monte Carlo n-particle extended simulation code (MCNPX, Ver. 2.6.0, National Laboratory, Los Alamos NM, USA). For both PET and SPECT scanners, lutetium-yttrium oxyorthosilicate (LYSO, density = 7.2 g/cm^3) was used as the scintillator material with size of 280 × 280 × 20 mm^3 [26,27]. The parallel hole collimator, composed of lead (density = 11.3 g/cm^3), had 70 holes with 2 mm diameter and 7 mm septum height [19,29]. The PET detector was designed as a ring type geometry with the same scintillation material as the SPECT detector. The size of the detector was 20 mm thick with 400 mm inner diameter. There were four kinds of water phantoms containing some cylindrical columns with either 364 keV or 511 keV radioisotope content for computer simulation. The number of the initial particles were 60 million per one projection in the SPECT simulations (total 32 projections). And the 1.92 billion initial particles were applied to the PET simulations. According to the National Electrical Manufacturers Association (NEMA), it is generally recommended that activity ratio between radioisotope region and background area was 4:1 [30]. However, in this study, radioisotope was placed only in the cylindrical column to minimize the effect of the background. Fig. 1 shows the detailed information for the geometry of these four phantoms which contained different cylindrical columns at different coordinates. The black circles mean the regions of the radioisotopes. Correctly, there are two kinds of the phantoms for the PET and two kinds of the phantoms for SPECT. Whole process of the image acquisition has been performed with MATLAB (2018b, Mathworks Inc., Sherborn, MA, USA).

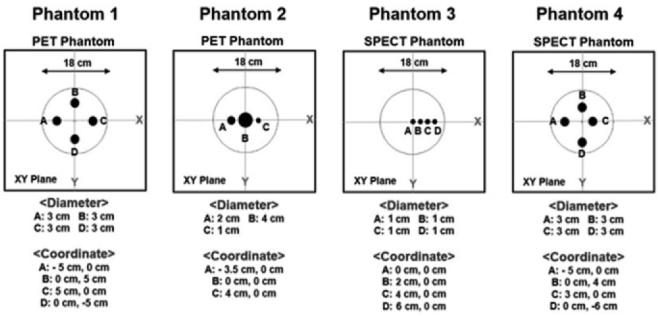

Fig. 1. Geometric information for all four types of water phantoms including the cylindrical column of the radioisotope region (black circle) at z = 0 plane for computer simulation. Each radioisotope region is tagged as an alphabet from A to C (or D). Phantom 1 and 2: PET phantoms, Phantom 3 and 4: SPECT phantoms.

2.2. Application of standard FBP reconstruction

To acquire the NM images using the standard FBP, the sinogram was firstly obtained from the PET and SPECT in the simulation. And it was then computed the inverse Fourier transform of each projection profile (Eq. (1)) [1,2]:

$$p' = F^{-1}[|k_r|P] \tag{1}$$

where $|k_r|$ is the high pass filter Ram-Lak, P is the projection file, F^{-1} is the inverse Fourier transform and p' is the inverse Fourier transform data. This process was applied to each k-space profile.

2.3. Application of GPU-based OSEM reconstruction

The NM imaging is of relatively low detection efficiency and requires fast image reconstruction capability [13–18] for the clinical application. In this study, OSEM algorithm with GPU (GPU-based OSEM) was applied for fast image reconstruction (Eq. (2)) [19]:

$$\lambda(new)_j = \frac{\lambda(old)_j}{\sum_{D_n}\sum_{D_m}\sum_{i\in S_L} C_{ij(nm)}} \sum_{D_n}\sum_{D_m}\sum_{i\in S_L} C_{ij(nm)} \left(\frac{Y_{i(nm)}}{\sum_K C_{ik(nm)}\lambda(old)_k}\right) \tag{2}$$

where λ is the image variable, C_{ij} is the system matrix, Yi is the count number of photons, D_n is the GPU domain length (horizontal thread number), D_m is the GPU domain length (vertical thread number). Because the S_L is the 'subset of part in sinogram' with

number L, the $\sum_i \in S_L$ means whole range of sinogram. And the *j* is a pixel number, the *k* is *j - 1* pixel number, the *i* is the detector unit.

The image reconstruction using the GPU-based OSEM was consistently performed with the 8 subsets and 5 iterations throughout this study.

2.4. Application of sigmoidal function profile optimization

In the process of sigmoidal function profile optimization (SFPO), the extracted profile from the simple spread image by the new sinogram could be optimized and then be changed as the ideal pattern of the profile. In order to optimize the profile, the 'weighting parameters' for each 'region' on the profile were required. To obtain the weighting parameters, the five SPECT images and the five PET images were additionally simulated using the same type of phantom with seven cylindrical columns of different sizes (Fig. 2). In order to acquire different image combinations from the reference phantoms, the signals for some specific regions were turned on/off during computer simulation. The two true images for both PET and SPECT, with all radioactive regions turned on, were also simulated to compare with the sample images of the phantom. The profiles were extracted from the all sample images according to the applied true images. The 786 reference profiles were extracted from the five reference SPECT images and from the five reference PET images. After the transformation of the extracted reference profile as the first derivative, the position of the reference profile was matched with the true profile which is extracted from the original phantom image. By comparing with the ideal patterns from true profiles (Fig. 3a), indices of each value in the profile were assigned as 'signal region' including the 'plateau region', 'signal to noise (S/N) interference', and 'noise region' according to the height of the differential profile. However, the actual differential curve looks like the curve in Fig. 3a. In that case, we are hard to correctly distribute where the terminal point of the signal region is. From the 786 profiles, we manually compared the position of each signal with the profiles of ideal pattern and analyzed the height of the differential profiles. And we found candidates for the signal region. Moreover, the clear signals were excluded from the candidates, the left signals from the candidates were distributed as the 'S/N interference'. Lastly, the other signals which didn't be selected as the candidates were distributed as 'noise'. In this process, some inclinations to differentiate the groups were found. From these 786 reference profiles, the gradient values based on various regions of signal, S/N interference, and noise were corresponding to the profile inclination of 49.3°–90° (±1.2°), 49.2°–16.8° (±2.3°), and 0°–16.7° (±0.9°) respectively. In the case of the S/N interference, its range started to rise to reach the signal region and vice versa. Although a definition of the S/N interference was most difficult in this study, we calculated the discrepancy values between the actual image profile and the reference profile together with the acquired average weighting parameters for S/N interference and signal region to be as an ideal pattern using sigmoidal function. And the image acquisition needed the spread image from the new sinogram

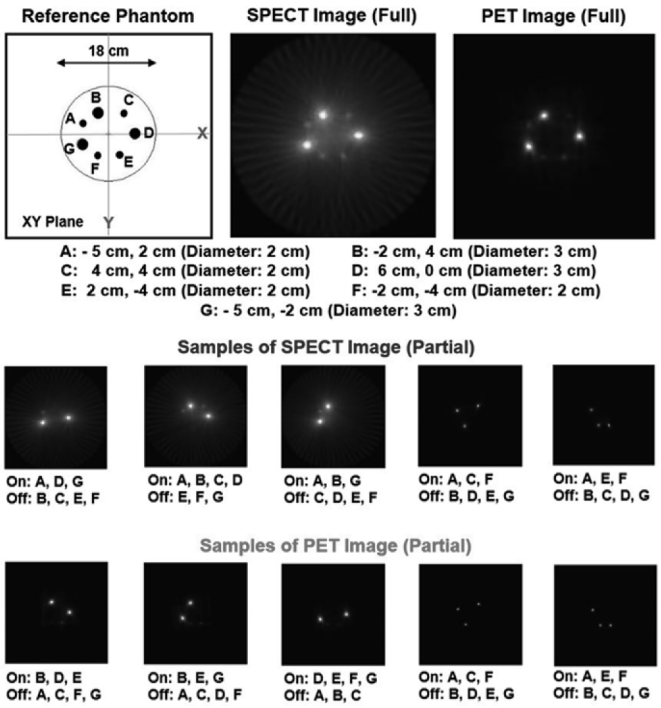

Fig. 2. Reference images for extracting the reference profiles. The water phantom contained seven circles of different sizes and locations. Images for all radioisotope regions included in the simulation were shown at top portion of the figure for both SPECT and PET images. Images by turning specific signal on/off were used to get the profiles, 5 images for SPECT and 5 images for PET were acquired from the reference phantom.

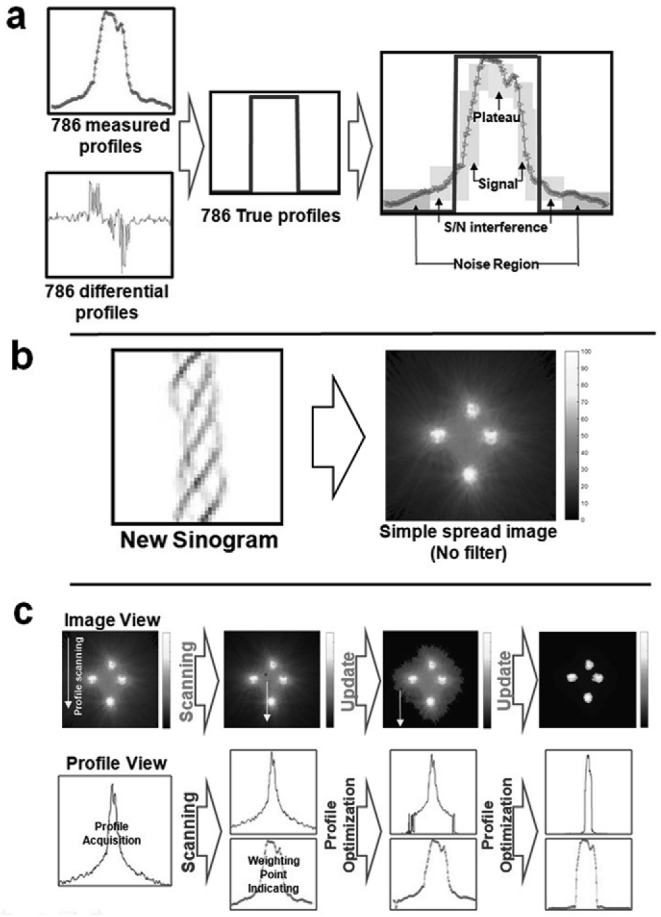

Fig. 3. Schematic process of NM imaging using sigmoid function profile optimization. To acquire the reference values for optimizing new profile, the 786 profiles acquired from 5 SPECT images and 5 PET images were used to define the 'region' on the profile (a). When the new sinogram is updated, it is changed as simple spread image (b). This simple image is updated to be the optimized image according to weighting parameters which is originated from the reference profiles. The final profile is close to ideal pattern of profile. Through the re-arrangement of the optimized profiles, the optimized reconstructed image is obtained (c). The downward arrow in the c does not match with the below profiles. This arrow is demonstrated to explain the direction of the 1D measurement at the moment for extracting the profiles from images.

without the application of any filters (Fig. 3b). The spread image was an image acquired by the simple back-projection using the sinogram without the application of any filters, processing. After the acquisition of the spread image, the 1D image profiles were extracted line by line with one direction on the image. In that case, the shape of profile looks like a rough mountain at the region of true signal. On the other hand, the profile of ideal pattern shows the perpendicularly convex shape. The extracted image profiles from the new spread image can be optimized by comparing with this profile of ideal pattern. According to iteration step, the shape of the rough mountain is gradually changing to the perpendicularly convex shaped in Fig. 3c. And we found the specific weighting parameters to optimize the profile according to the shape of the sigmoidal function by manual comparison. There were three weighting parameters W_i ($i = 1$ to 3) to optimize the profiles. These weighting parameters would be multiplied to each value in the original profile according to the updated process, and correspondingly the updated profile would be changed as like a shape of sigmoidal curve. The W_1 (0.071 according to the slope) was assigned to the noise region. If the gradient values were identified to the noise region, the W_1 was applied to the profile's value as the noise region's index. The W_2 (0.071–1.384 according to range from 16.8° to 90°) was assigned to S/N interference and signal region. They were applied to the profile's values at S/N interference's and signal region's indices. These regions would then be changed like middle point of the sigmoidal function. The last weighting parameter was W_3 (1.066) was applied to the image plateau region. The general transformation for the $profile(r)_{new}$ from the previous profile $P(r)$ is summarized as (Eq. (3)):

$$Profile(r)_{new} = \begin{cases} P(r)\cdot W_1 & r \text{ within noise region} \\ P(r)\cdot W_2 & r \text{ within } S/N \text{ \& signal region} \\ P(r)\cdot W_3 & r \text{ within plateau region} \end{cases} \quad (3)$$

where r was a pixel value in one profile.

This r could be assigned at any of the three regions according to the conditions as above (Eq. (3)). The gradient of plateau region was similar to the gradient of noise region. However, when the profile was scanned, the gradients after (or before) the signal region was regarded as noise region. With these weighting parameters, the updated process was continuously iterated to achieve the true images. The iterative process would terminate when the difference of normalized signal intensity between the maximum value in S/N interference and minimum value in S/N interference was above the 50% inflection point of the sigmoidal curve. Each image was needed an average of 3–5 iterations. Actually, there is a clear difference between the standard FBP and the method what we proposed. The image reconstruction using the standard FBP has a filter process on the sinogram after Fourier transformation. However, our proposed method does not include neither the filter process nor the Fourier transformation. The proposed method is originated from the optimization of the profile on the 1D spatial space. Basically, the optimization should have criteria to deduct the best solution, these criteria have been extracted from the 786 profiles acquired from the 10 reference images.

2.5. Image analysis

To quantitatively analyze the region containing radioisotope, the noise, contrast and signal-to-noise ratio (SNR) were acquired from using the region of interest (ROI) for each region and for the background. We set the ROIs according to the number of radioisotope regions of each phantom. The size of each ROI was set as 70% of physical diameter of radioisotope region. The number and size of ROI on background region were also set equal to those of ROIs on radioisotope region. The position was similar to that of the radioisotope region, and the measured values were averaged. The contrast and SNR were calculated as (Eqs. (4) and (5)):

$$Contrast = \frac{|S - B|}{|S + B|} \quad (4)$$

$$SNR = \frac{S}{B_{SD}} \quad (5)$$

where S was the average signal in the region containing the radioisotope, B was the average background signal, and B_{SD} was the standard deviation of the background.

Secondly, the full width half maximum (FWHM) was measured from each peak on the image profiles acquired from the reconstructed images according to the type of the reconstruction algorithm. When the profiles were normalized as the highest point on the peak with 100%, the distance between the former point of 50% and the latter point of 50% on the peak was calculated. Moreover, in order to evaluate the degree of the dispersion, the penumbra was also measured from the all images. All of images including even reference images were adjusted as 210 × 210 matrix with the size of 40.9 cm × 40.9 cm. Thus, the size of the one pixel on the image was 1.95 mm. The number of pixels from 20% to 80% of relative signal intensity on the half of the peak was counted to measure the penumbra.

Lastly, both the sizes of each regions and the coordinate of each region on the reconstructed images were measured. Although the size of signal is hard to be defined on the reconstructed image due to the penumbra, in order to exclude the effect of the penumbra, the criteria for defining range of the size was fixed as over the signal

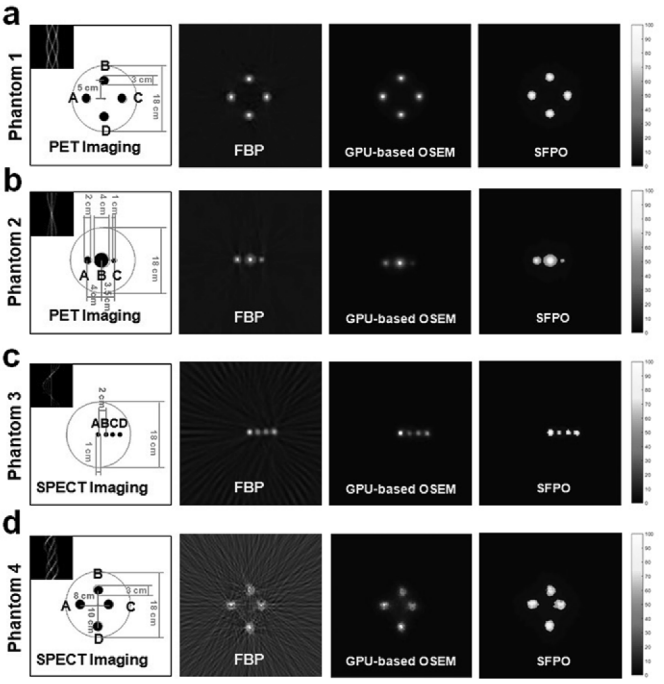

Fig. 4. Reconstructed images using standard FBP (second column), GPU-based OSEM (third column) and SFPO (fourth column) using the same sinogram with the four phantoms of different coordinates for the radioisotope regions of same intensity (a and b for PET imaging, c and d for SPECT imaging). The geometric information of each phantom is reported at first column. FBP: filtered back projection, GPU: graphics processing unit, OSEM: ordered subset expectation maximization, SFPO: sigmoidal function profile optimization.

intensity of 10% on the normalized image. If the signal intensity of 10% is hard to be found due to high level for the noise, the size was measured by using a trend line at the bottom of the peak. And the coordinates of each region were found by identifying the point of the highest signal within each region.

3. Results and discussion

Fig. 4 shows the images using the reconstruction algorithms of standard FBP, GPU-based OSEM and SFPO. There were two types of imaging acquisitions of PET (Fig. 4a and b) and of SPECT (Fig. 4c and d). The four phantoms were configured to reflect the effect that could occur when acquiring PET and SPECT images. In the phantom 1, the region of the radioisotope with same diameter were arranged at regular intervals. Phantom 2 had three regions with different diameter along the X axis. Phantom 1 and 2 for PET image were constructed to evaluate the effect of overlapping angles and the relative small region discrimination. In the case of SPECT phantom, in order to evaluate the effect of detector ration, small regions of phantom 3 that could be difficult to distinguish along the X axis were arranged, and the region of the radioisotope of the phantom 4 were divided into irregular intervals. The first column at the left in Fig. 4 shows the original shape of the phantom including the regions of the radioisotope for imaging. There were three or four radioisotope uptake regions labeled as A, B C and D (except Fig. 4b) and displayed in spherical patterns in the phantoms. The second column indicated the reconstructed images using the standard FBP reconstruction algorithm. In the cases of Fig. 4c and d, the streak artifact was also observed in the image using the standard FBP reconstruction algorithm. These artifacts were due to the lack of sufficient projection numbers [1,2]. If the projection number was insufficient to reconstruct images with the standard FBP algorithm, a streak artifact could be resulted as the limitation of the standard FBP reconstruction algorithm. The third column shows the reconstructed images using the reconstruction algorithm of the GPU-based OSEM. One of the advantages of the OSEM algorithm is its ability the for image reconstruction with fewer projections [14–16]. The sinogram used in this study was in purpose to provide an insufficient projection number to reconstruct the images. Nonetheless, the images constructed by using the GPU-based OSEM demonstrated very clear signal regions with low noise levels for the different radioisotope configuration, because this reconstruction algorithm was based on the equation of probability distribution to reduce the noise level [19,20]. However, when there was a little bit weak signal (Fig. 4b and c), the true signal could not be resolved by OSEM. The degradation process during the iteration was due to the low probability of signal distribution. Additionally, the size of the reconstructed signal region was observed being smaller than the actual size of the radioisotope region. Lastly, the reconstructed images using the SFPO were demonstrated at last column of Fig. 4. Overall image shows the clearness of the signal intensity, the sharpness of the signal edge, and dramatically low level for the noise. In the PET image (phantom 1, 2), the edge of the signal region was clearly distinguished overall, however a slight distortion occurred in the SPECT image (phantom 3, 4). This result may indicate that the radioisotope region is overfitting. This study has limitations that make it difficult to calculate theoretical values such as standardized uptake value (SUV). This phenomenon is assumed to be overfitting the center portion of the radioisotope region. Therefore, experimental verification using phantom having theoretical value such as SUV or reference value is necessary to overcome this limitation in our study.

Table 1 shows the results for the contrast and SNR as a type of the reconstruction algorithm on each region as shown in Fig. 4. In order to show simply the difference of SNR according to reconstruction algorithm, the all of values for SNR in Table 1 were normalized by using the maximum value of the SNR in this table. Hence, the highest SNR will be demonstrated as 100. Because of the noise generated by the standard FBP algorithm, the contrast increases from 1.17 to 2.63 times and the SNR increases from 5.75 to 57.20 times as observed from the case of SFPO. When the results of OSEM are compared to those of the SFPO, the intensity of the noise region on the OSEM profile was not much different than that of the SFPO. The contrast increased from 1.09 to 2.65 times. However, because the signal intensity of the OSEM decreased, the results of SNR for the SFPO increased from 1.53 to 28.46 times. When the SFPO is compared with other two methods, the contrast and SNR were improved overall. Especially, it can be seen that the difference of the contrast was remarkable at the results in the phantom 4. In the case of SNR, the values in the result for the standard FBP reported relatively low level because it didn't perform any image denoising processes. In addition, the difference of the SNR between for SFPO and for other methods is noticeable at the results for the phantom 3 and 4.

Table 1
Contrast and normalized signal to noise ratio (SNR) for each region having a radioisotope as the type of the reconstruction algorithms. FBP: filtered back projection, GPU: graphics processing unit, OSEM: ordered subset expectation maximization, SFPO: sigmoidal function profile optimization.

		Contrast values			Normalized SNR		
			GPU-based	SFPO		GPU-based	SFPO
Phantom	Region	FBP	OSEM		FBP	OSEM	
1	A	0.78	0.83	0.91	5.62	57.57	93.46
	B	0.77	0.85	0.92	5.47	64.81	99.39
	C	0.77	0.84	0.92	5.54	59.02	97.05
	D	0.77	0.85	0.92	5.35	63.94	100.00
2	A	0.65	0.86	0.90	9.12	13.49	89.70
	B	0.62	0.89	0.91	8.23	17.71	100.00
	C	0.64	0.78	0.86	8.56	8.01	66.58
3	A	0.76	0.91	0.96	17.37	19.69	100.00
	B	0.62	0.79	0.92	10.38	7.76	48.65
	C	0.63	0.83	0.94	10.54	9.72	64.49
	D	0.70	0.86	0.95	13.54	11.91	78.63
4	A	0.32	0.52	0.84	1.60	3.02	85.96
	B	0.35	0.58	0.86	1.73	3.64	94.16
	C	0.38	0.62	0.86	1.87	4.10	100.00
	D	0.33	0.55	0.86	1.63	3.33	93.23

Fig. 5 shows the image profiles measured vertically and horizontally from all images as reconstructed by standard FBP, GPU-based OSEM and the SFPO of using the same sigmoidal profile function. The trend of standard FBP images shows high intensity at the signal regions and even high level for the noise. Moreover, the trend regarding the high level for the noise is remarkably demonstrated in Fig. 5e and f, where the noise level is over 20%. The representative strong point of OSEM is the low noise in the NM image. However, the weak intensity for the true signal can be suppressed with the distribution probability [35]. This trend is noticeable at the 60th pixel in Fig. 5c and at the 35th pixel in Fig. 5d. Thus, the difference of level between the signal and noise is only 10–20%. The peak of the signal region, on the image profile acquired using standard FBP and GPU-based OSEM image, are relatively narrow in signal peak. The boundary area between the signal and noise regions was smooth. Moreover, the higher intensity shows the thinner peak shape. From the images as obtained from the SFPO, it shows the high intensity for the signal and low level for the noise as the advantages of the reconstruction algorithm. Normally, the noise level on SPECT image is higher than that of PET

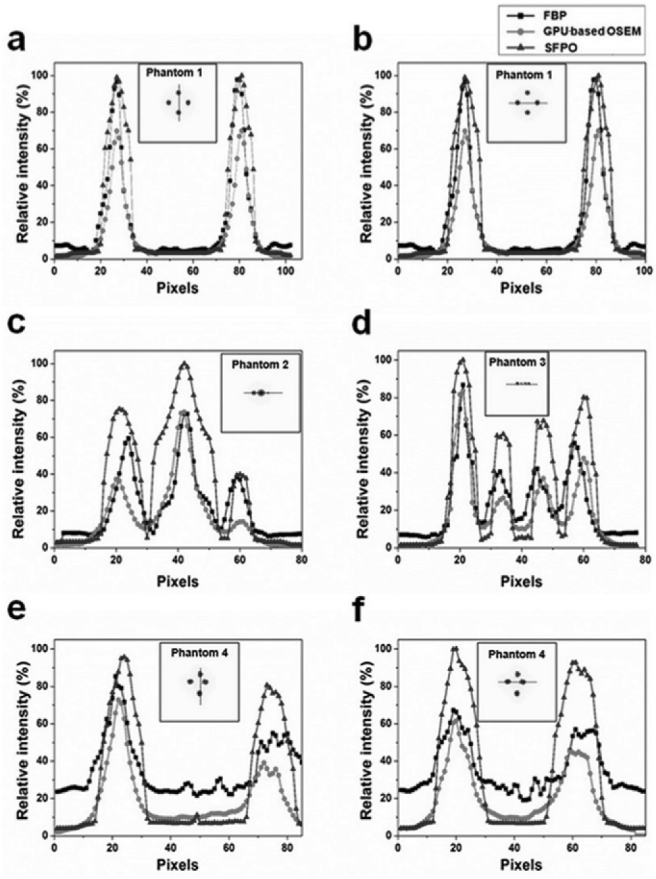

Fig. 5. The extracted image profiles from the images in Fig. 4 a and b show the vertical and horizontal images profiles including 2 regions for the phantom 1. c and d show the image profiles for the phantom 2 and the phantom 3, respectively. e and f show the vertical and horizontal images profiles including 2 regions for the phantom 4. The black line including square marker is the image profile for the standard FBP. The red line including circle marker is the image profiles for the GPU-based OSEM. The blue line is the image profiles for the SFPO. (For interpretation of the references to colour in this figure legend, the reader is referred to the Web version of this article.)

image due to streak artifact by the back-projection when the number of projections is low. Moreover, because Fig. 5e and f shows the radioisotope regions of a little bit large size than the regions in Fig. 5d, the more correct deposition events for the true signal are required to show the difference of the almost same level between the signal level and the noise level with case in Fig. 5d. For this reason, the noise levels in Fig. 5e and f shows the higher than other cases. Especially, the SNR is improved by distinguishing the signal from the SPECT image well, which is consistent with the result in Table 1.

Table 2 shows the results for both the FWHM and the number of pixels for the penumbra. The results in case of SFPO show the highest values from all cases. On the other hand, although the FWHMs for standard FBP and for GPU-based OSEM have same trend each other, somewhat low FWHMs were reported. In addition, the lowest number of the pixels for the penumbra was measured from all cases for the SFPO. The highest number of pixels was 6 from case of the standard FBP, it means that the range of the penumbra was maximum 11.7 mm. The low FWHM and the high number of the pixels for the penumbra lead the large degree of the dispersion. It means that the shape of the signal peak is vast different with the ideal pattern of the signal.

Table 3 presents the results of the measurement for the size and the coordinate of each region on the reconstructed images. Overall trend of the measured size is almost same with the trend of the actual size. Some cases from even case of the SFPO reported the over size. Although the over size from the case of standard FBP is originated from the high noise level as well as the broad penumbra, the over size from the case of SFPO is induced by the overfitting for the optimization. The maximum difference of the size between the actual size and the measured size was reported as 1.14 cm. The minimum size was 0.08 cm. The start point of the coordinate on the image was an edge for the top of left side at the image. Although there is very little difference among the coordinate according to the method of the reconstruction, the maximum difference of the number of pixels was 6.

There have been a lot of studies to develop the algorithm for the image reconstruction. Moreover, some researchers have tried to

Table 2
Full width half maximum (FWHM) for each peak on the profiles, and the number of the pixels for the penumbra range (from 20% to 80%).

		FWHM (cm)			Number of pixels for penumbra range (20% −80%; Pixel: 1.95 mm)		
			GPU-based	SFPO		GPU-based	SFPO
Phantom	Region	FBP	OSEM		FBP	OSEM	
1	A	1.30	1.18	2.55	4	4	1
	B	1.25	1.10	2.32	5	4	2
	C	1.35	1.10	2.54	4	4	2
	D	1.19	1.08	2.52	6	5	2
2	A	1.14	1.07	1.89	5	5	2
	B	1.21	1.21	3.41	5	4	2
	C	0.94	0.91	0.96	4	3	1
3	A	0.69	0.78	0.96	3	3	1
	B	0.68	0.63	0.72	3	4	2
	C	0.65	0.65	0.81	4	4	2
	D	0.66	0.61	0.83	4	4	2
4	A	1.21	1.08	2.52	4	3	2
	B	1.19	1.11	2.67	4	3	1
	C	1.32	1.21	2.74	4	3	1
	D	1.22	1.10	2.50	5	3	2

Table 3
Sizes of each region on the reconstructed images and the coordinates of the highest signal intensity within each region on the reconstructed images. The range of size was defined as the distance between the former point of 10% and the latter point of 10% on the signal peak.

		Size of regions (<10%; cm)			Average coordinate for regions (210 by 210 matrix)		
			GPU-based	SFPO		GPU-based	SFPO
Phantom	Region	FBP	OSEM		FBP	OSEM	
1	A	3.11	2.73	2.92	78,107	78,108	80,105
	B	3.11	2.92	2.92	104,81	106,81	106,78
	C	2.92	2.73	3.11	130,108	134,108	133,105
	D	3.11	2.92	2.92	104,134	108,135	106,132
2	A	2.53	2.14	2.53	85,101	82,105	84,107
	B	3.31	3.50	3.89	105,101	103,105	104,107
	C	1.75	1.56	1.36	122,101	123,105	124,107
3	A	1.95	1.95	2.14	104,103	105,105	105,106
	B	1.95	2.14	1.36	116,104	119,105	119,106
	C	1.56	1.95	1.75	128,103	132,105	132,106
	D	1.75	1.95	2.14	140,103	145,105	145,106
4	A	3.11	2.92	2.92	77,105	79,107	78,105
	B	3.30	3.11	2.92	105,84	106,87	106,86
	C	2.92	2.92	3.11	121,106	122,109	121,107
	D	3.11	2.92	3.11	104,139	105,140	104,138

apply the deep learning to the reconstruction of the images which has the improved quality than the performance of the image using the conventional reconstruction methods. There is a representative study to show similar results with the results in this study. Ida et al. progressed the deep learning based PET image reconstruction using a deep encoder-decoder [36]. They used 2D images of 98,000, and deep neural network of U-net type to acquire the PET image. When the results in this study is compared with that of above study, there are some representative differences. First, the proposed method for imaging in this study does not be based on the technique using the machine learning or the deep learning. The optimization skill is used to change the profile ideally. Second, the proposed method in this study can cover the SPECT image reconstruction as well as the PET image reconstruction. Because this method has approached forward 1D profiles, not the image. Third, there is a difference of number of the images for learning (or reference). In this process, some strong and weak points can be reported on the comparison. For the strong points, the image reconstruction time was very short (<1 s) for all of cases. Moreover, the high computing power does not be required, such as for the deep learning. Because there is no heavy computation by comparing with the conventional reconstruction, the required time for the image reconstruction was extremely short. And we used only very small number of images for the reference. This number cannot be used to even machine learning. However, the better image quality was shown. Lastly, this method has been proposed to cover the image reconstruction for both the SPECT and the PET. Obviously, the image reconstruction of the PET is different with image reconstruction of the SPECT. Even the image reconstruction using the deep learning should be considered as the different construction for the design of the algorithm. However, because the method of profile optimization in this study does not recognize the signal as the 2D image, it does not be influenced from the type of the imaging module. On the other hand, the proposed method in this study has clear weak points. Firstly, the parameters were found manually from the reference images. Surely this stage can be replaced by the deep learning. It looks like a stage of 'learning' for the deep learning. However, this process is the providing a 'knowledge' rather than the 'learning'. In this study, we needed human's judgement for the signal using only small cases rather than the machine's judgement using big data. It does not require the heavy scale data to solve the problem. There is another weak point by connecting above weak point. Basically, because the proposed method is based on the computational algorithm, not the machine learning, the formulaic results should be acquired. However, these results can be drastically changed according to the quality of the reference. It means that if the human's judgement is continuously wrong, the quality of image will be extremely different. However, this weak point can be covered by some experts.

4. Conclusions

In this study, we have acquired the NM image using sigmoid function profile optimization which is a different method with the conventional type for the image reconstruction. By comparing with other reconstruction methods such as standard FBP and GPU-based OSEM, the SFPO demonstrated that better quality for the reconstructed image with the results of the quantitative analysis.

Declaration of competing interest

The authors declare that they have no known competing financial interests or personal relationships that could have appeared to influence the work reported in this paper.

Acknowledgement

This research was supported by Radiation Technology Research and Development program (Grant No. 2017M2A2A7A01070973) through the National Research Foundation of Korea (NRF) funded by the Ministry of Science, Information and Communication Technologies (ICT).

References

[1] L. Hongbo, W. Kun, T. Jie, Postreconstruction filtering of 3D PET images by using weighted higher order singular value decomposition, Biomed. Eng. Online 15 (2016) 102.
[2] S. Cherry, J. Sorenson, M. Phelps, Physics in Nuclear Medicine, Elsevier Health Sciences, 2012.
[3] M. Law, C. Tang, Capability of 3D ordered subset expectation maximization (OSEM) reconstruction algorithm in performing half-time myocardial perfusion imaging studies, in: Radiological Society of North America, USA, Nov 30 – Dec 5, 2014.
[4] P. Bruyant, Analytic and iterative reconstruction algorithms in SPECT, J. Nucl. Med. 43 (2002) 1343–1358.
[5] O. Grosser, D. Kupitz, J. Ruf, et al., Optimization of SPECT-CT hybrid imaging using iterative image reconstruction for low-dose CT: a phantom study, PloS One 10 (2015), e0138658.
[6] D. Yang, D. Xing, H. Gu, Y. Tan, L. Zeng, Fast multielement phase-controlled photoacoustic imaging based on limited-field-filtered back-projection algorithm, Appl. Phys. Lett. 87 (2005) 194101.
[7] C. Floyd, R. Jaszczak, R. Coleman, Inverse Monte Carlo: a unified reconstruction algorithm for SPECT, IEEE Trans. Nucl. Sci. 32 (1985) 779–785.
[8] H. Liu, M. Guo, Z. Hu, P. Shi, H. Hu, Nonlinear dual reconstruction of SPECT activity and attenuation images, PloS One 9 (2014), e106951.
[9] T. Moon, The expectation-maximization algorithm, IEEE Signal Process. Mag. 13 (1996) 47–60.
[10] X. Yu, S. Chen, Z. Hu, et al., Sparse/low rank constrained reconstruction for dynamic PET imaging, PloS One 10 (2015), e0142019.
[11] J. Cui, X. Liu, Y. Wang, H. Liu, Deep reconstruction model for dynamic PET images, PloS One 12 (2017), e0184667.
[12] Y. Vardi, L. Shepp, L. Kaufman, A statistical model for positron emission tomography, J. Am. Stat. Assoc. 80 (1985) 8–20.
[13] T. Yokei, H. Shinohara, H. Onishi, Performance evaluation of OSEM reconstruction algorithm incorporating three-dimensional distance-dependent resolution compensation for brain SPECT: a simulation study, Ann. Nucl. Med. 16 (2002) 11–18.
[14] H. Hudson, R. Larkin, Accelerated image reconstruction using ordered subsets of projection data, IEEE Trans. Med. Imag. 13 (1994) 601–609.
[15] K. Lange, M. Bahn, R. Little, A theoretical study of some maximum likelihood algorithms for emission and transmission tomography, IEEE Trans. Med. Imag. 6 (1987) 106–114.
[16] J. Ollinger, Maximum-likelihood reconstruction of transmission images in emission computed tomography via the EM algorithm, IEEE Trans. Med. Imag. 13 (1994) 89–101.
[17] F. Beekman, H. De-Jong, S. Van-Geloven, Efficient fully 3-D iterative SPECT reconstruction with Monte Carlo-based scatter compensation, IEEE Trans. Med. Imag. 21 (2002) 867–877.
[18] H. Shin, M. Kim, S. Kim, et al., Quantitative analysis of prompt gamma ray imaging during proton boron fusion therapy according to boron concentration, Oncotarget 9 (2018) 3089.
[19] D. Yoon, J. Jung, K. Hong, K. Lee, T. Suh, GPU-based prompt gamma ray imaging from boron neutron capture therapy, Med. Phys. 42 (2015) 165–169.
[20] C. Chou, Y. Dong, Y. Hung, et al., Accelerating image reconstruction in dual-head PET system by GPU and symmetry properties, PloS One 7 (2012), e50540.
[21] H. Shin, D. Yoon, J. Jung, M. Kim, T. Suh, Prompt gamma ray imaging for verification of proton boron fusion therapy: a Monte Carlo study, Phys. Med. 32 (2016) 1271–1275.
[22] N. Freedman, D. Schechter, M. Klein, et al., SPECT attenuation artifacts in normal and overweight persons: insights from a retrospective comparison of Rb-82 positron emission tomography and Tl-201 SPECT myocardial perfusion imaging, Clin. Nucl. Med. 25 (2000) 1019–1023.
[23] E. Garcia, SPECT attenuation correction: an essential tool to realize nuclear cardiology's manifest destiny, J. Nucl. Cardiol. 14 (2007) 16–24.
[24] S. Tong, A. Alessio, P. Kinahan, Noise and signal properties in PSF-based fully 3D PET image reconstruction: an experimental evaluation, Phys. Med. Biol. 55 (2010) 1453.
[25] P. Zanzonico, An Overview of Nuclear Imaging, Radiopharmaceutical Chemistry, 2019.
[26] K. Hong, Y. Choi, J. Jung, et al., A prototype MR insertable brain PET using tileable GAPD arrays, Med. Phys. 40 (2013), 042503.
[27] L. Qin, H. Li, S. Lu, D. Ding, G. Ren, Growth and characteristics of LYSO (Lu2(1_x_y)Y2xSiO5: cey) scintillation crystals, J. Cryst. Growth 281 (2) (2005) 518–524.
[28] A. Gaitanis, G. Kontaxakis, G. Spyrou, et al., Studying the properties of the

updating coefficients in the OSEM algorithm for iterative image reconstruction in PET, Comput. Methods Progr. Biomed. 99 (2010) 219–229.
[29] P. Slomka, T. Pan, D. Berman, G. Germano, Advances in SPECT and PET hardware, Prog. Cardiovasc. Dis. 57 (2015) 566–578.
[30] H. Shin, H. Sheen, H. Lee, et al., Digital Imaging and Communications in Medicine (DICOM) information conversion procedure for SUV calculation of PET scanners with different DICOM header information, Phys. Med. 44 (2017) 243–248.
[31] A. Fogliata, R. Garcia, T. Knöös, et al., Definition of parameters for quality assurance of flattening filter free (FFF) photon beams in radiation therapy, Med. Phys. 39 (2012) 6455–6464.
[32] S. Lebron, B. Lu, G. Yan, et al., Parameterization of photon beam dosimetry for a linear accelerator, Med. Phys. 43 (2016) 748–760.
[33] Y. LeCun, Y. Bengio, G. Hinton, Deep learning, Nature 521 (2015) 436–444.
[34] D. Silver, J. Schrittwieser, K. Simonyan, et al., Mastering the game of Go without human knowledge, Nature 550 (2017) 354.
[35] J. Nuyts, S. Stroobants, P. Dupont, et al., Reducing loss of image quality because of the attenuation artifact in uncorrected PET whole-body images, J. Nucl. Med. 43 (2002) 1054–1062.
[36] I. Häggström, C. Schmidtlein, G.Campanella T. Fuchs, DeepPET: a deep encoder–decoder network for directly solving the PET image reconstruction inverse problem, Med. Image Anal. 54 (2019) 253–262.